Vector diffraction from subwavelength optical disk structures: two-dimensional modeling of near-field profiles, far-field intensities, and detector signals from a DVD

Wei-Chih Liu and Marek W. Kowarz

Rigorous two-dimensional vector-diffraction patterns of a focused beam incident on an optical disk, specifically, a digital versatile disk (DVD), are examined both in the near field and in the far field. An efficient finite-difference frequency-domain method is developed for calculating the electromagnetic fields in the neighborhood of subwavelength dielectric and metallic structures. The results of vector-diffraction theory are compared with those of scalar-diffraction theory for pressed DVD features that consist of pits or of bumps. The sum (data) and difference (tracking) signals from a split photodetector are also calculated for different disk features and for different polarizations. The subwavelength features of a DVD result in considerable vector-diffraction effects both in the near-field profiles and in the detector signals, depending not only on the polarization of illumination but also on whether the features are pits or bumps. This paper provides important insight into the vector-diffraction effects encountered in high-density optical data storage systems. © 1999 Optical Society of America

OCIS codes: 210.0210, 050.1960, 210.4590.

1. Introduction

Fast progress in nanotechnology and in microelectronics fabrication has led to numerous engineered structures that, in size, are comparable with or smaller than the wavelength of visible light. For optical data storage systems smaller spot size is a key requirement for high-density recording. In fact, the digital versatile disk (DVD), which is becoming the new standard for multimedia distribution, has a minimum feature size that is smaller than the readout laser wavelength (see Section 4). Since optical storage systems can employ various polarizations of incident light, and since features on the DVD have dimensions smaller than the wavelength of the laser light, the reflected light signals are expected to show a strong polarization dependence. Theoretical modeling and analysis of these polarization effects require rigorous vector-diffraction theory for dealing with material boundaries.

Inspired by the exciting development in near-field optics and in near-field microscopy,[1–4] certain new types of optical storage system make use of near-field signals from the disk surface to surpass the conventional resolution limit and to achieve a substantially higher storage capacity. From the early stages of near-field optical microscopy there were numerous proposals for data storage systems that use the tip of an optical fiber[5] or a subwavelength slit-type probe[6,7] to pick up near-field signals from optical disks. A promising alternative to this approach is the solid immersion lens, which employs an objective lens that flies tens of nanometers from the surface of the storage medium.[8–11] Detailed understanding of these systems requires the study of near-field profiles on the disk surface. Although there are numerous modeling studies of near-field optical systems, little published research on near-field optics[7,12,13] has focused on high-density optical data storage systems.

To investigate vector diffraction from optical disks (or the closely related problem of vector diffraction from a grating with a finite number of periods), various numerical algorithms such as the finite-difference time-domain (FDTD) method,[14,15] mode-

W.-C. Liu (wcliu@pas.rochester.edu) is with the Rochester Theory Center for Optical Science and Engineering, University of Rochester, Rochester, New York 14627-0171. M. W. Kowarz is with the Integrated Materials and Microstructures Laboratory, Imaging Research and Advanced Development, Eastman Kodak Company, Rochester, New York 14650-2015.

matching methods,[7,16–20] the boundary element method,[21–24] and the integral method[25–27] have been used. Previous research on the subject can be subdivided into several types of configuration: plane fields incident on perfectly conducting structures[17,20] or dielectric structures,[21] plane fields incident on realistic metallic structures,[13,24,25,28] focused fields incident on perfectly conducting structures,[18,19,22,26,27] and focused fields incident on realistic metallic structures.[14–16,23,29] Until recently,[26,27,29] little attention was paid to the modeling of the DVD configuration, which has features smaller than the wavelength of the laser light that would cause considerable vector-diffraction effects in near-field distributions, far-field intensities, and detector signals. Most of the previous studies modeled various optical disk configurations with considerably larger features.

Several of these studies emphasized especially the detector signals generated by an optical disk. Depine and Skigin[28] illustrated that there are notable differences between the signals from a perfect conductor and those from a highly conducting metal. Kobayashi[18] used vector-diffraction theory to treat a focused, truncated Gaussian beam [numerical aperture (NA) is 0.6] incident on a rectangular, perfectly conducting grating. He examined the dependence of the readout and servo signals on the incident polarization, the depth of grooves and pits, and the feature size. Gerber and Mansuripur[30] experimentally observed that, when the incident medium is air, the detector signals from metal-coated surfaces differ significantly for the two incident polarizations. Judkins et al.[15] simulated a two-dimensional rewritable optical disk with the FDTD method and experimentally validated the tracking performance.

In this paper we discuss the modeling of a DVD optical storage system with rigorous vector-diffraction theory and present results for the near-field distributions, the far-field intensities, and the detector signals. For this purpose we developed an efficient FDFD method for calculating the electromagnetic fields in the neighborhood of realistic dielectric and metallic subwavelength structures to a high accuracy.[29] Our two-dimensional simulation treats the rigorous vector diffraction of a focused polarized Gaussian beam that interacts with two-dimensional aperiodic pressed disk structures. We explore different DVD configurations that contain either pits or bumps in the disk surface (see Section 4). The signals from a split detector show a strong dependence on the polarization of the incident light and on the geometry of the features on the disk. Our results demonstrate that the vector diffraction effects of the DVD configuration are more significant than those of earlier optical formats discussed in previous studies. Most notable is the large difference between the results for a disk with pressed pits versus those for one with pressed bumps.

2. Numerical Methods

Since we are interested in steady-state phenomena, the electromagnetic field can be assumed to be time

harmonic and the FDFD method can be used to solve the time-harmonic Maxwell equations. In source-free media that are nonmagnetic, isotropic, and inhomogeneous the time-harmonic Maxwell equations may be written as

$$\nabla \times \mathbf{E} = i\omega\mathbf{H},$$
$$\nabla \cdot (\epsilon\mathbf{E}) = 0,$$
$$\nabla \times \mathbf{H} = -i\omega\epsilon\mathbf{E},$$
$$\nabla \cdot \mathbf{H} = 0, \tag{1}$$

where $\mathbf{E}$ is the electric field, $\mathbf{H}$ is the magnetic field, ϵ is the complex electric permittivity, ω is the angular frequency, and a time dependence of $\exp(-i\omega t)$ has been assumed. The information about material properties is included in ϵ. With elimination of the magnetic field the Maxwell equations become

$$\nabla^2\mathbf{E} + \omega^2\epsilon\mathbf{E} = \nabla(\nabla \cdot \mathbf{E}), \tag{2}$$

$$\nabla \cdot (\epsilon\mathbf{E}) = 0. \tag{3}$$

Equation (2) is in the form of a coupled general Helmholtz equation and is the main equation we worked on. With properly imposed boundary conditions and grid geometry the divergence equation is satisfied automatically.[31,32] To solve Eq. (2), we combine several techniques to develop an efficient and (to our knowledge) a novel FDFD method.

A. Concus–Golub Iteration

Concus and Golub[33] have proposed an iteration scheme based on a fast cyclic-reduction Helmholtz solver[34–36] for the repeated solution of Helmholtz-like equations. This method exploits the sparcity of the discrete Helmholtz equation and can handle separable equations of the form

$$\nabla^2 E(y, z) + \omega^2\epsilon_0(z)E(y, z) = f(y, z), \tag{4}$$

where $f(y, z)$ is an arbitrary source term. This equation can describe the layered optical disk structure. The cyclic reduction method can produce fast direct solutions at $O(3n^2 \log n)$ for an $n \times n$ matrix, has a small memory requirement, and can be well parallelized.[37,38]

In Eq. (2) each component has the form of a general Helmholtz equation

$$[\nabla^2 + \omega^2\epsilon(y, z)]E_i = \nabla_i(\nabla \cdot \mathbf{E}), \tag{5}$$

where the source term is the component from $\nabla(\nabla \cdot \mathbf{E})$. The unknown electric field can be solved with the Concus–Golub iteration method. Specifically, for the kth iteration we use the expression

$$(\nabla^2 + \omega^2\epsilon_0)E_i{}^k = -\omega^2[\epsilon(y, z) - \epsilon_0]E_i{}^{k-1} + \nabla_i(\nabla \cdot \mathbf{E}^{k-1}). \tag{6}$$

It has been demonstrated with finite differences[33] that the number of necessary iterations can vary dramatically depending on the function $\epsilon(y, x)$. Usually, the smoother $\epsilon(y, x)$ is, the faster the rate of

convergence. When the Concus–Golub iteration method does not converge, we use the conjugate gradient method to overcome this difficulty.

B. Conjugate Gradient Method

Conjugate gradient methods are probably the most popular iterative techniques for solving systems of linear equations. They are often referred to as subspace iteration methods, because they solve a system of linear equations $A x = b$ by minimization of quadratic functionals in Krylov subspaces, which are spanned by a series of vectors generated by repeated multiplication by A.

The Concus–Golub iteration can be used as a good preconditioner in conjunction with a robust restarted general minimal residual conjugate gradient method[39] to fully solve for electric fields to a very high accuracy.[40] From numerical experiments it was found that the internal iterations that correspond to the Concus–Golub preconditioner do not need to converge to reach optimum computing performance.[40]

C. Radiation Boundary Condition

To solve the Maxwell equations in an infinite domain numerically, for example, in diffraction or scattering problems, it is usually necessary to limit the computation to a finite domain and to impose a radiation boundary condition on the outer edge of the numerical grid. The purpose of the radiation boundary condition is to absorb the scattered or radiated fields when they arrive at the grid edge and to simulate boundless free space.

The Engquist–Majda[41,42] and the Mur[43] radiation boundary conditions and their variations have been frequently used in FDTD calculations. Although their original formulations are derived in FDTD framework, it is straightforward to adapt them to frequency-domain format. In this paper we use Higdon's variation of the second-order finite-difference radiation boundary condition:[44,45]

$$\left[\left(\cos\alpha_1 - \frac{i}{k}\frac{\partial}{\partial z}\right)\left(\cos\alpha_2 - \frac{i}{k}\frac{\partial}{\partial z}\right)\right]E = 0, \qquad (7)$$

where α_1 and α_2 are the optimal angles for minimal reflection. The $\hat{z}$ direction is the primary direction of wave propagation in our case, and the angles α_1 and α_2 are zero. This boundary condition is equivalent to the second-order Engquist–Majda radiation boundary condition,[44] but it is better suited for the cyclic reduction method, because it involves the derivative in only one direction.

3. Configuration

The surface of a DVD-ROM disk (ROM means read-only memory) consists of a polycarbonate substrate covered with aluminum with tracks of pressed pits (Fig. 1). We consider a simplified two-dimensional model to simulate the vector diffraction from these pits. When the geometry of the structure is two dimensional, the problem decomposes into two inde-
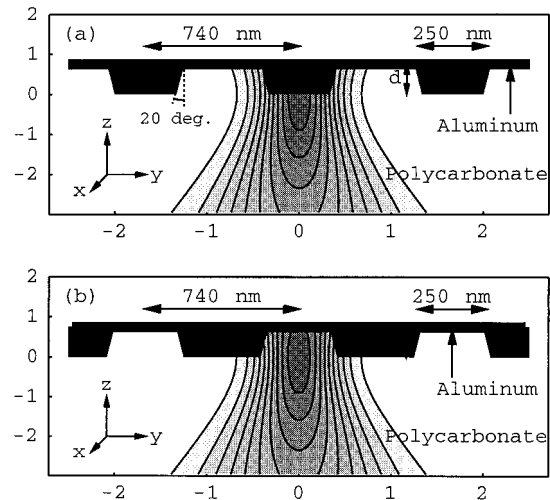

Fig. 1. Cross section of the two-dimensional model of the DVD surface. The axes are in units of wavelengths. (a) Disk with pits, (b) disk with bumps.

pendent polarizations. We define TE polarization to be the case when the electric field is perpendicular to the plane of incidence and parallel to the pits and TM polarization to be the case when the electric field is in the plane of incidence.

The complex indices of refraction are $n = 1.6$ for the polycarbonate substrate and $n = 1.5 + 7.8\,i$ for the aluminum reflection layer. The wavelength in vacuum of the incident laser light is $\lambda = 650$ nm. Consequently, the wavelength in the polycarbonate substrate is $\lambda_s = 406$ nm. The normal-incident two-dimensional Gaussian beam has a FWHM of approximately 600 nm, which corresponds to an objective lens NA of 0.6.

In the numerical calculations there are five pits on the disk surface. The (average) width of the pits is 250 nm, the track pitch or distance between the pits is 740 nm, and the sidewall angle is 20 deg. The depth of the pits is varied between 0.1 and 0.8 λ_s, and the position of the laser relative to the center pit is varied between 0 and 1 λ_s. To study the effects of different geometries on the signals, we also examined diffraction from five bumps [see Fig. 1(b)].

The computation box is set to 5 λ_s ($\approx 2.03\ \mu$m) in the z direction and 12 λ_s ($\approx 4.87\ \mu$m) in the y direction. There are 40 grid points in each wavelength located in a Yee cell[46] in two-dimensional space. We would like to emphasize the importance of using a Yee cell geometry, since it maintains consistency between the discrete forms of the first and the second derivatives in Maxwell equations (2) and (3).

4. Near Fields

Figures 2 and 3 show color maps of the electric fields in the neighborhood of the center pit for two typical cases. The pit heights are $d = 0.3\,\lambda_s$ (≈ 120 nm) and $d = 0.6\,\lambda_s$ (≈ 240 nm), respectively. The field shown here is the total field, which includes both the incident and the diffracted fields. For TE illumination

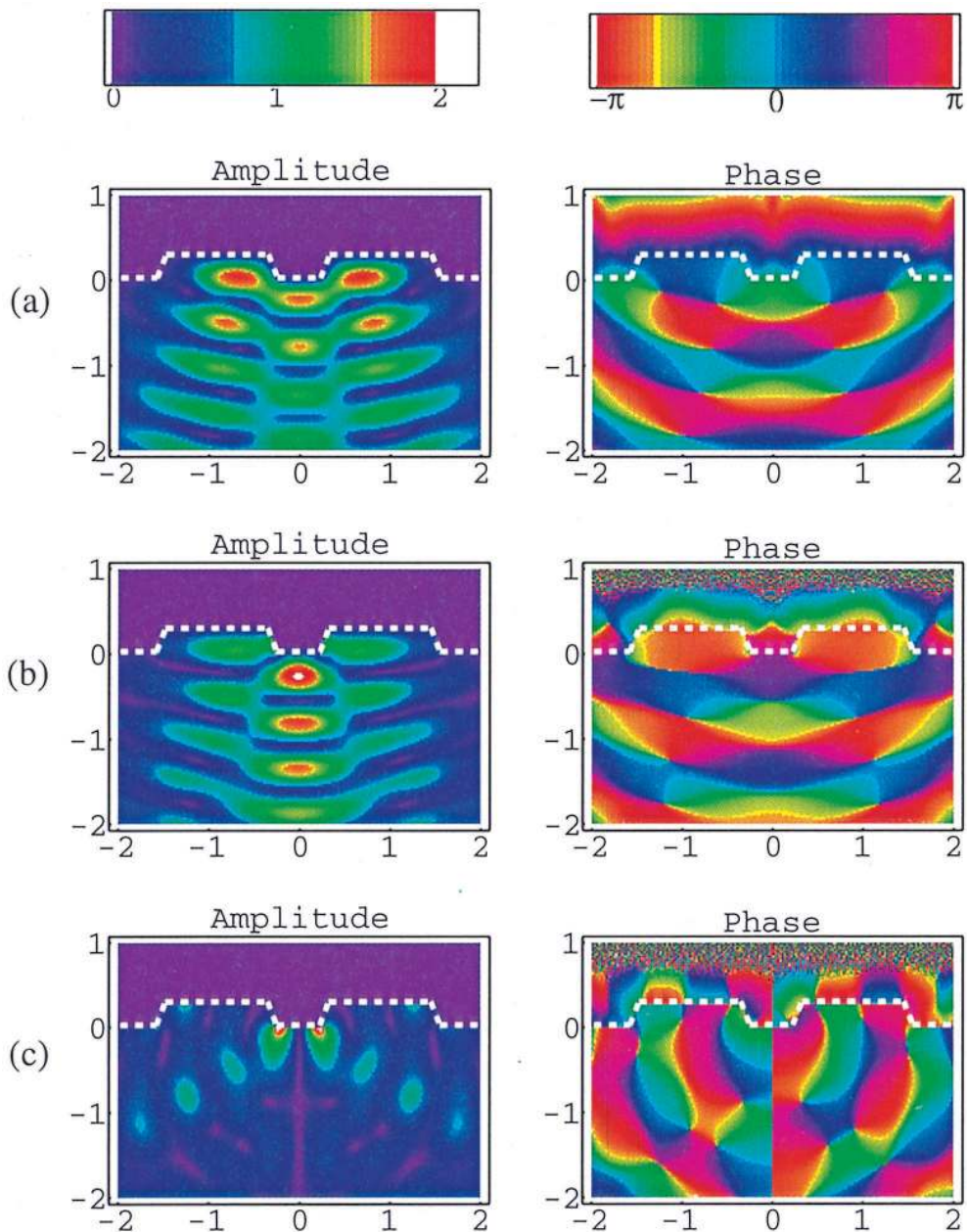Fig. 2.   Near-field profile of (a) the E_x component for TE illumination, (b) the E_y component for TM illumination, (c) the E_z component for TM illumination.   The pit height is 0.3 λ_s.   The unit of length here and in subsequent figures is the wavelength in the substrate $\lambda_s = 406$ nm.

there is only an E_x component present, whereas for TM illumination there are both E_y and E_z components that are coupled together.   The first case, $d = 0.3$ λ_s, shows strong destructive interference that sends much of the reflected light outside the NA of the objective lens, whereas the second case, $d = 0.6$ λ_s, shows constructive interference that causes mirrorlike reflection.   The phase graphs depict clearly the phase fronts, indicative of the direction of wave propagation.   It should be noted that, in the TM case, the E_z component shows propagation in the y direction.   This indicates that evanescent fields contribute to this component, though the magnitude of

these evanescent fields is small, especially for the 0.6 λ_s pit.

Figures 4–7 show the amplitude of the electric fields near the middle pit (or bump) for pit heights (or bump heights) between 0.1 and 0.8 λ_s ($\approx$40–320 nm). We show only the E_y component of the TM case, because it is generally the dominant component for this polarization.   The flatness of the surface of constant amplitude in these figures is related to the degree of constructive or destructive interference in the reflected field.   It is therefore possible to anticipate the far-field behavior in Section 5 directly from the near-field results.
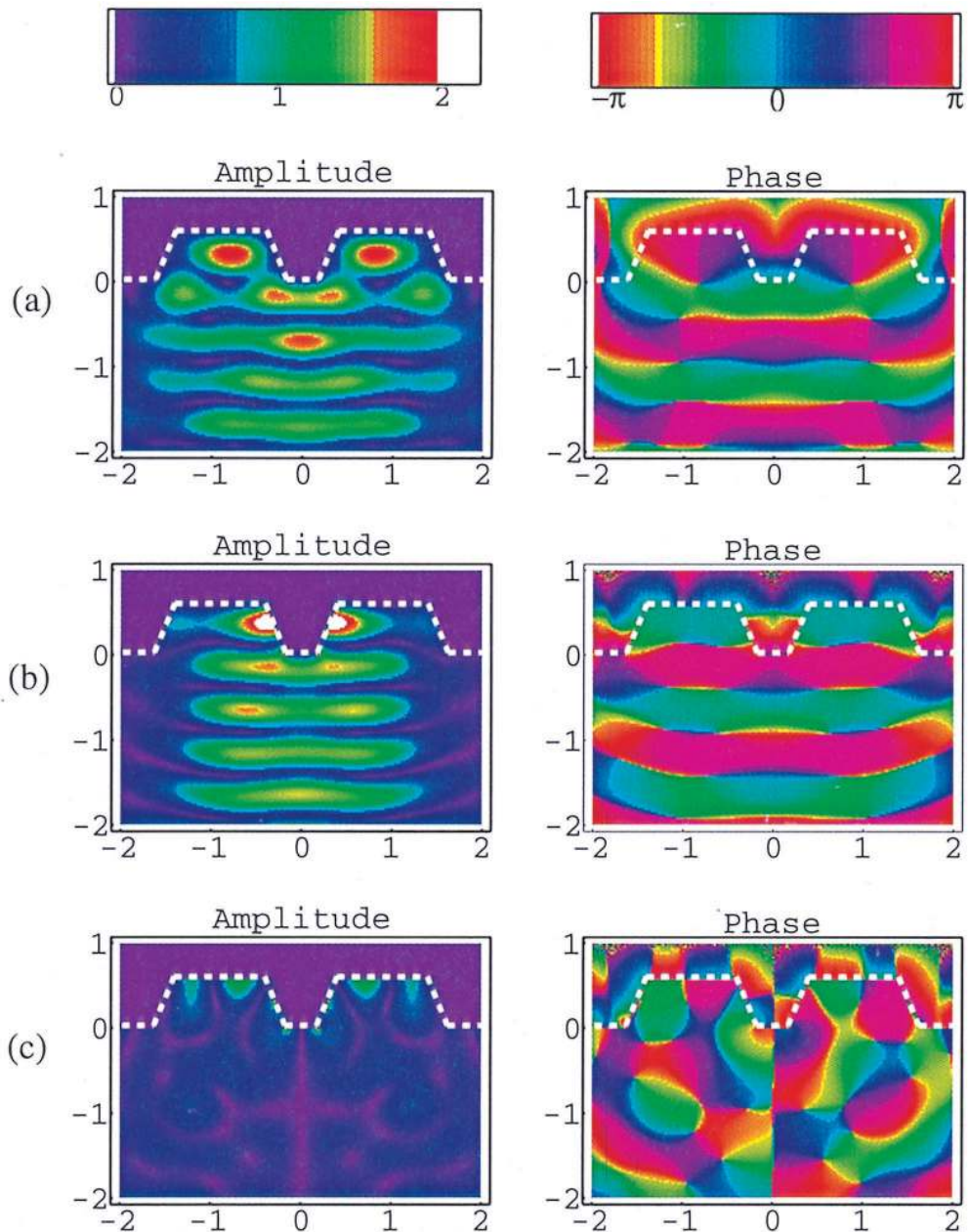
Fig. 3. Near-field profile of (a) the E_x component for TE illumination, (b) the E_y component for TM illumination, (c) the E_z component for TM illumination. The pit height is $0.6 \, \lambda_s$.

In Fig. 4, for TE illumination, there are strong peaks, not only in front of the pit but also adjacent to it. With increasing pit height a visible resonant mode emerges in the space between the pits. The resonant mode is even stronger for the bump configuration in Fig. 6. The main difference between the two configurations is that there is a single resonant peak in the bump case, whereas there are two resonant peaks on opposite sides of the center pit in the pit case. The TM near-field profiles are significantly different from the TE ones. Initially, for small pit heights, the amplitude of the primary component of the electric field is nearly the same for both polarizations and is also quite similar to that for the bump

configuration. For small feature heights one expects all four cases to be similar to the predictions of scalar theory. However, the similarity diminishes with increasing pit height. It is interesting to note that, for the bump configuration with TM illumination, a node begins to appear in the resonant mode when the bump height is larger than $0.3 \, \lambda_s$, and a second node appears when the bump height is larger than $0.7 \, \lambda_s$.

It is well known that in near-field optics measurements the fields detected by a small tip are proportional to those found in the absence of the tip.[47,48] We can easily observe what a near-field probe would pick up from Figs. 4–7 (assuming the polycarbonate substrate is removed). Madrazo and Nieto-Vesperinas
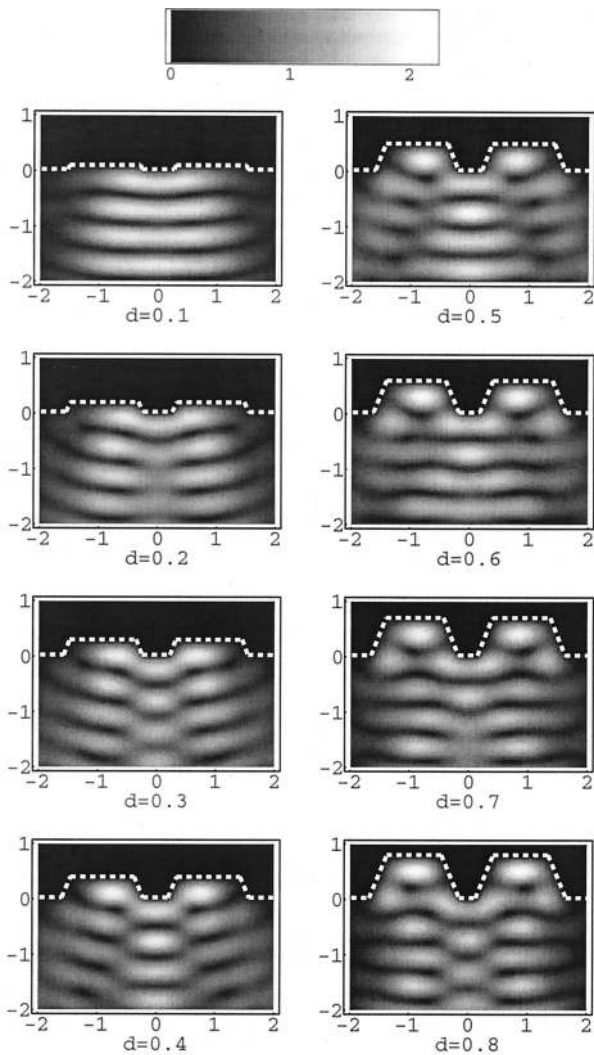
Fig. 4. Near-field profile of the amplitude of the E_x component for TE illumination. The pit heights are varied between 0.1 and 0.8 λ_s.
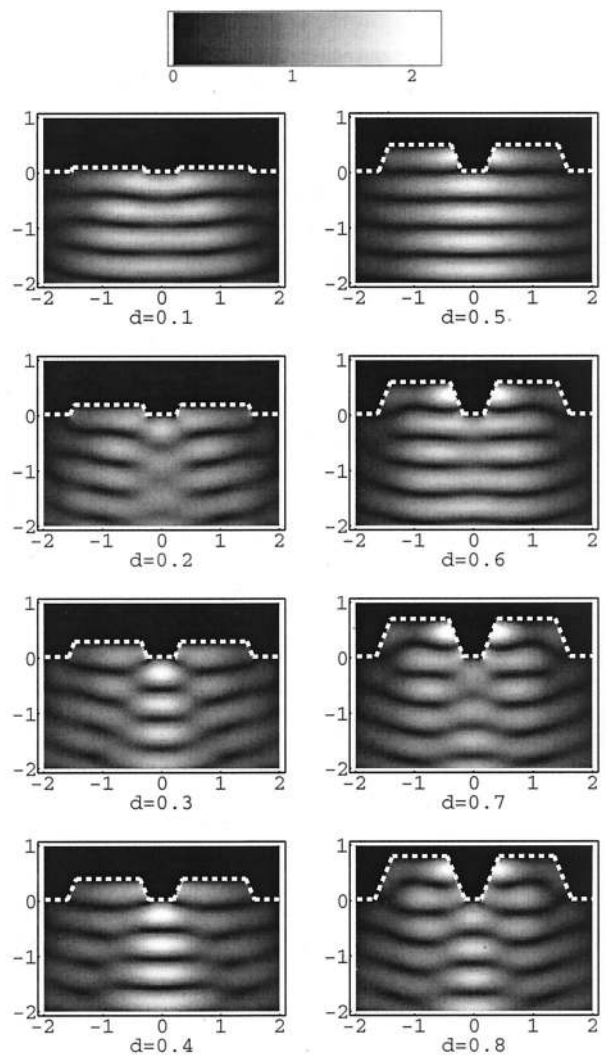

Fig. 5. Near-field profile of the amplitude of the E_y component for TM illumination. The pit heights are varied between 0.1 and 0.8 λ_s.

calculated the near fields of two adjacent deep Gaussian-shaped grooves.[13] They found that at a plane $z = -z_0$, where z_0 is a small fraction of the wavelength, the near-field intensity distribution closely follows the groove profile in the TE case (s polarization in their paper), but not for the TM case (p polarization in their paper). Our results confirm their conclusion for both the bump and the pit configuration when the heights are small. However, with increasing bump/pit height, the resonance peaks in the TE case are difficult to identify with the position of the bump or pit. This is especially true for $d \approx 0.5\ \lambda_s$ when constructive interference masks the presence of a feature. The very narrow groove used in their calculations is probably responsible for this difference.

5. Far Fields

To calculate the far fields, the near-field pattern is sampled inside the mesh and the far-field distribution is calculated with a simple transform based on the Franz variation of Huygens' principle with a far-

zone approximation to the Green's function. For example, for the E_x component,

$$E_x(\theta) = A(R) \int dy \exp(iky \sin \theta)\left(E_x \cos \theta + \frac{\partial E_x}{\partial z}\right),$$

(8)

where θ is the angle with respect to the normal direction, A is a proportionality coefficient that depends only on the distance R to the observation point, and $k = \omega/c$. The transform takes the transverse components of the scattered field along a plane above the surface of the disk and projects those components onto a circle in the far field.

Figure 8 shows the far-field intensities in the normal direction for the TE, TM, and scalar cases as a function of pit and bump height. Both polarizations have first minima around a pit height of 0.3 λ_s ($\approx$240 nm), which is therefore the optimal height for maximum contrast. The effective phase depth for TE polarization is less than in scalar-diffraction theory,
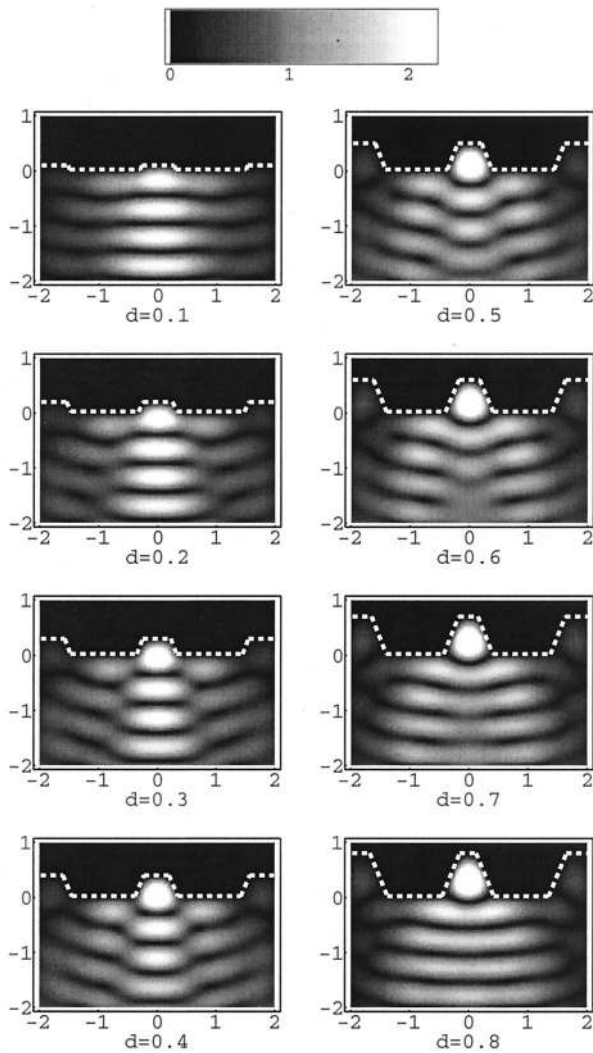
Fig. 6. Near-field profile of the amplitude of the E_x component for TE illumination. The bump heights are varied between 0.1 and 0.8 λ_s.

Fig. 7. Near-field profile of the amplitude of the E_y component for TM illumination. The bump heights are varied between 0.1 and 0.8 λ_s.

whereas for TM polarization it is nearly the same as scalar theory. As the pit height becomes larger, the deviation between the TE results and scalar theory increases. For the bump configuration the TM and the scalar results remain similar to the pit configuration, but the TE case exhibits an even more significant delay in phase depth. The significant phase depth difference between the TE and the TM cases can be related to the near-field resonant modes.[26,27] It is interesting to note that, for both pit and bump configurations, the scalar-theory maximum that occurs at 0.5 λ_s is significantly smaller than the corresponding maximum for vector theory. Our calculations indicate that this difference is due to a large contribution from evanescent waves in scalar theory at this height. This artifact is not present in vector theory.

The angular distribution of the far fields is shown in Fig. 9. It should be noted that, when diffraction in the normal direction is small, two strong sideband peaks contain most of the diffracted light intensity.
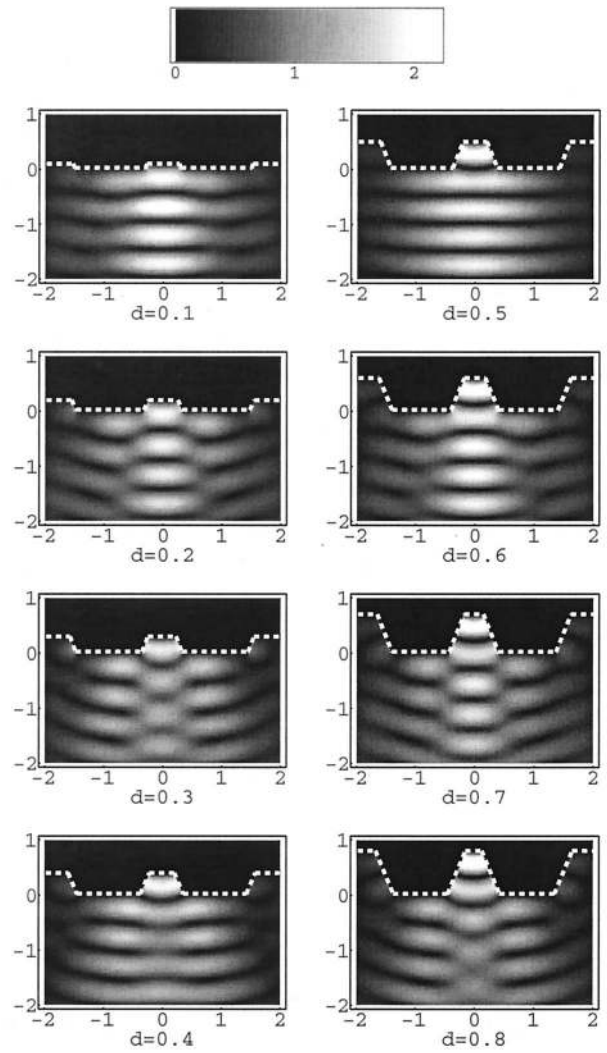
Since there are five pits or bumps in our configuration and since the FWHM of the incident Gaussian beam is less than the distance between adjacent pits or bumps, the angular distributions are similar to those for an infinite grating. The deviation from the infinite grating case reflects the effect of the finite number of pits or bumps in our configuration. We found that, when the focal point moves from the center to one side, this deviation becomes larger. Furthermore, the TM case is more sensitive to the actual number of pits or bumps than the TE case, probably owing to strong surface current effects. In Section 6 we show that the difference signal is particularly sensitive to the finite number of pits or bumps.

In a usual DVD player the incident field is circularly polarized. The results for the far-field intensity of circularly polarized illumination is approximately the average of the TE and the TM cases. Therefore, the intensity and the phase depth for circularly polarized illumination is expected to be more similar to scalar theory. However, because of the difference of phase
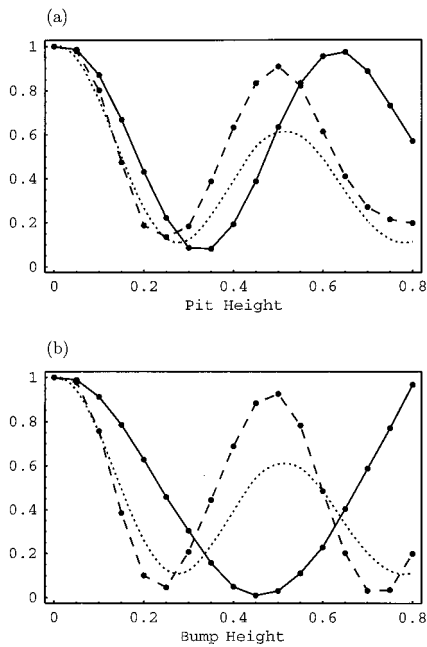
Fig. 8. Far-field intensities in the normal direction as functions of (a) pit and (b) bump heights. Solid curve, TE illumination; dashed curve, TM illumination; dotted curve, scalar theory.

depth between the TE and the TM cases, the ellipticity and the direction of the polarization ellipse of the diffracted field would change relative to those of the incident field.

6. Detector Signals

The irradiance pattern in the pupil of the objective lens after reflection from the disk can be obtained directly from the angular distribution of the far fields. (In three-dimensional optical disk diffraction this pupil irradiance distribution is often called the baseball pattern.[49–51]) We investigated the dependence of the signals from a split detector in the pupil plane on the polarization of the incident beam and on the geometrical parameters of the disk. The sum of the two split cells, $I_{SUM} = I_1 + I_2$, provides the data signal, and the difference, $I_{DIF} = I_1 - I_2$, provides a push–pull signal for tracking servo control. When the beam is precisely centered on the pit/bump, the irradiation distribution is symmetric with respect to the detector halves, so I_{DIF} is zero. When the beam moves away from the exact center, an asymmetrical distribution of intensity arises on the detector, producing a nonzero difference signal. It should be noted that, in practice, push–pull tracking is not used on DVD-ROM disks, because these disks are optimized for maximum data contrast, which results in poor push–pull tracking performance. Instead, differential phase detection provides tracking servo control in the DVD-ROM. However, the push–pull tracking signal is still of interest here, because it is used on writable DVD's and because it is sensitive to asymmetries in the far-field pattern.

Figure 10 shows the results from our calculations for the sum signal from different pit and bump heights. The detector signals are quite different for
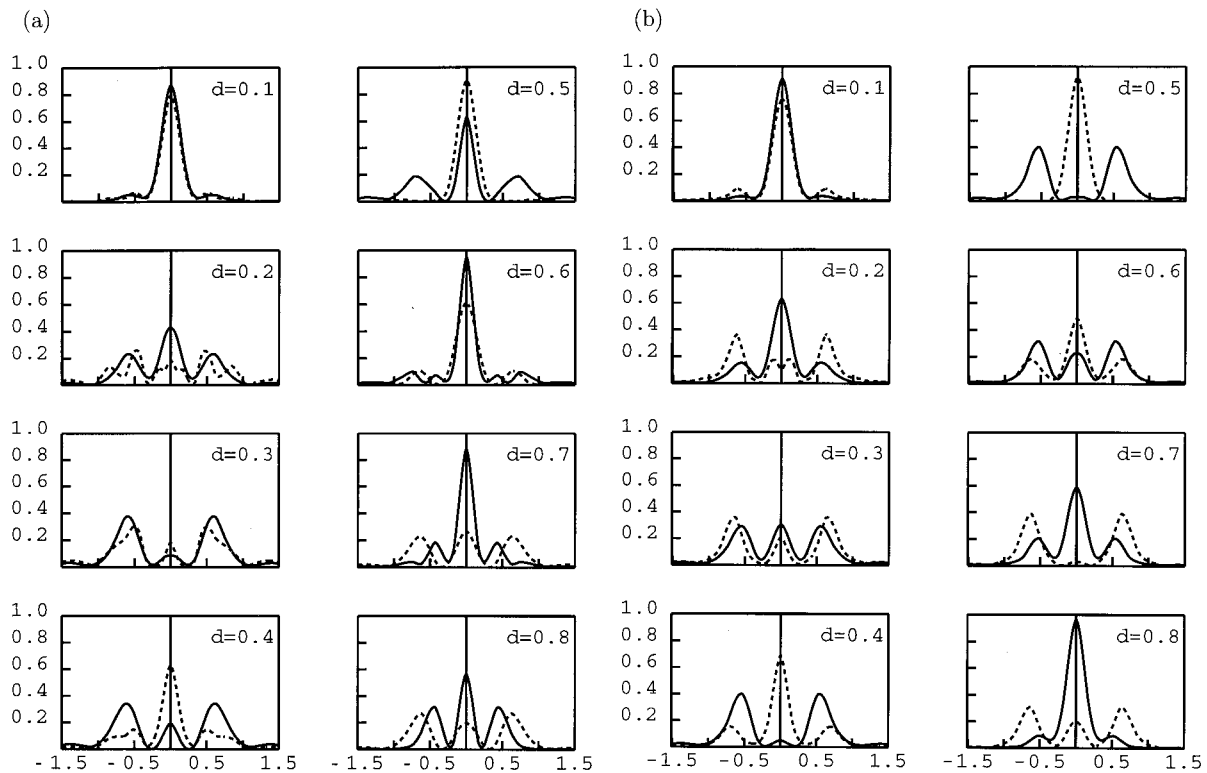

Fig. 9. Angular distributions of far-field intensities for pit and bump heights varied from 0.1 to 0.8 λ_s. (a) Pit configuration, (b) bump configuration. Solid curve, TE illumination; dashed curve, TM illumination. Horizontal axis, diffracting angle in polycarbonate.
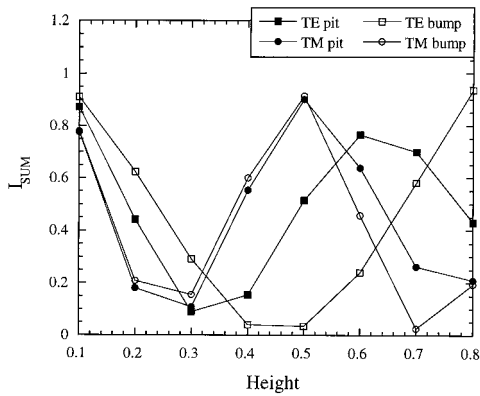
Fig. 10. I_{SUM} as a function of pit and bump heights.

the two incident polarizations and are also different for the two feature geometries, i.e., pit and bump. As might be expected, the sum signals are similar to the far-field intensities in the normal direction shown in Fig. 8 and change only slightly when the focal point moves away from the center. Figures 11 and 12 show contour plots of the difference signal as a function of both pit/bump height and displacement of the beam with respect to the center of the pit/bump. The distance between adjacent pits or bumps is 1.82 λ_s. Therefore the magnitude of I_{DIF} should be maximized when the displacement of the focus is approximately 0.45 λ_s and should come back to zero when the displacement is 0.91 λ_s. For TE polarization I_{DIF} comes back to zero precisely halfway between two tracks, as would be expected for an infinitely long array of pits or bumps. However, we found that for TM polarization I_{DIF} does not return to zero exactly at the center point, which shows asymmetry due to

the finite-number pits or bumps in our configuration. This asymmetry may also imply a higher cross-talk level for TM polarization than for the TE.

In the pit configuration the first tracking signal amplitude maximum occurs at a height of ~0.2 λ_s for the TE case and ~0.15 λ_s for the TM case. In the bump configuration the first maximum is at ~0.25 λ_s for the TE case and at ~0.1 λ_s for the TM case. The large difference between the tracking signal results for the two polarizations of incident light is consistent with previous research, especially since we use a metal surface and a NA of 0.6 in these calculations. For comparison scalar theory predicts an optimal tracking height of 0.125 λ_s for all four cases. Note the periodic sign reversal that occurs with increasing height.

7. Conclusion

The near-field diffraction and the far-field diffraction of a focused laser beam incident on a two-dimensional DVD surface has been investigated with what to our knowledge is a new FDFD method. The results of vector-diffraction theory have been compared with those of scalar-diffraction theory, and we have observed that different polarizations of the incident beam lead to significant differences in the detector signals and also potentially in the level of cross talk between tracks. Another important deviation from the scalar-diffraction theory is that there are significant differences between the results for a pit and those for a bump. These differences are especially important for experimental work aimed at optimizing DVD's for readout and for tracking. As data densities are increased further, vector-diffraction effects will become even more important with the higher
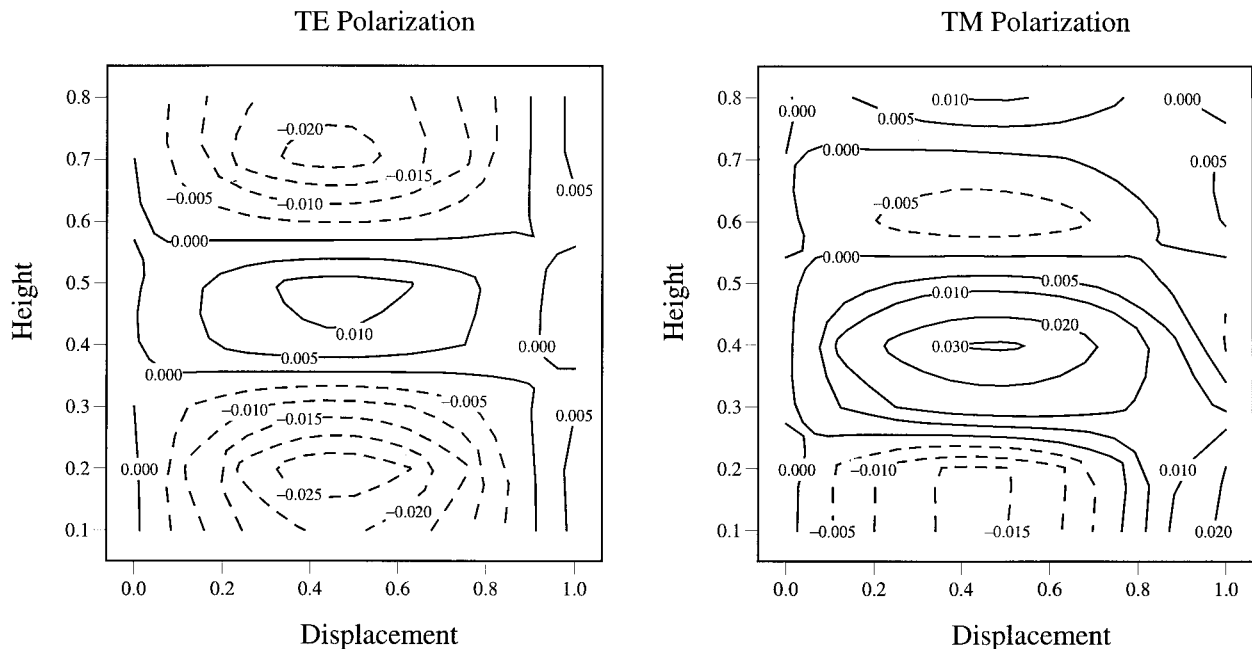

Fig. 11. Contour plot of I_{DIF} as a function of pit height and displacement of the focus point of the incident Gaussian beam relative to the center pit for the TE and the TM cases.
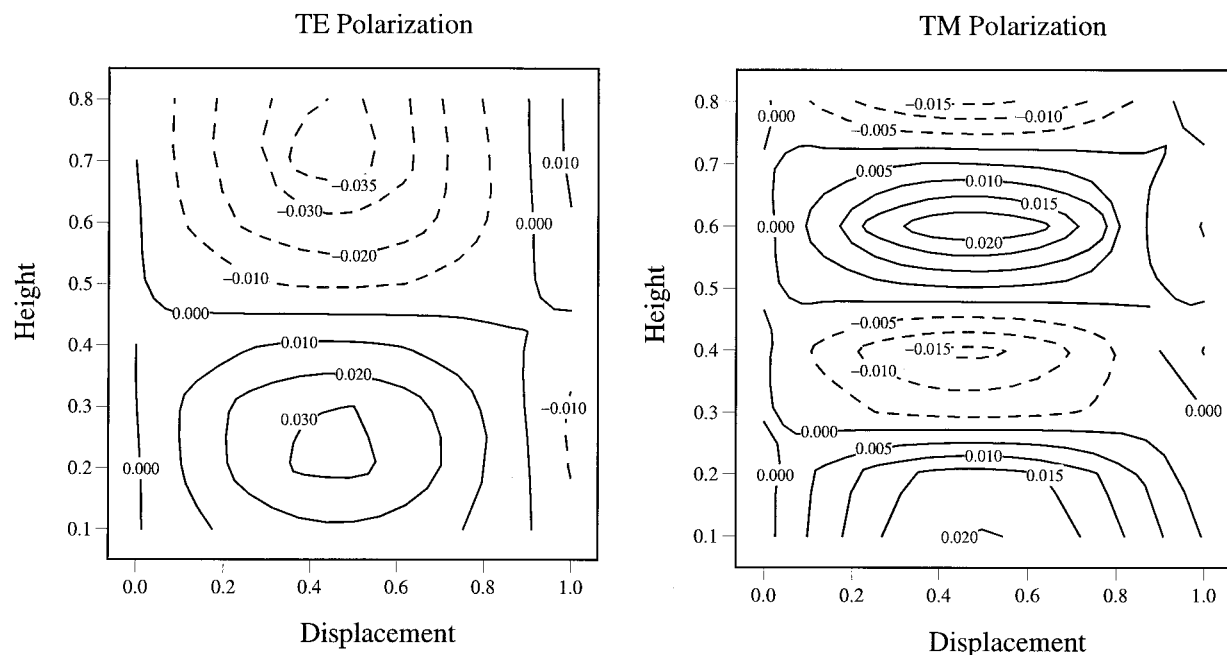
TE Polarization　　　　　　　　　　　　TM Polarization

Fig. 12.   Contour plot of I_{DIF} as a function of bump height and displacement of the focus point of the incident Gaussian beam relative to the center bump for the TE and the TM cases.

NA's and smaller disk features used in these systems. For rigorous analysis of light from high-NA systems that interact with subwavelength three-dimensional disk features a three-dimensional model is under development.

Although the choice of data density and servo schemes associated with a particular new optical storage device will be determined by several variables, it is essential that detailed modeling of the various interactions be performed. With numerical simulation one can more readily evaluate the alternatives while independently varying different parameters. This is not easily or cheaply accomplished with an experimental setup, and therefore numerical modeling provides an important aid in the design of optical storage systems.

This research can serve as a design tool for future optical storage systems and can also be applied to near-field calculations of other small-scale optical systems. With various new approaches to optical data storage systems that pick up near-field signals from the surface of the storage medium it is essential to gain more insight about near-field profiles.

References

 1. D. Courjon and C. Bainier, "Near field microscopy and near field optics," Rep. Prog. Phys. **57,** 989–1028 (1994).
 2. C. Girard and A. Dereux, "Near-field optics theories," Rep. Prog. Phys. **59,** 657–699 (1996).
 3. M. A. Paesler and P. J. Moyer, *Near-Field Optics: Theory, Instrumentation, and Applications* (Wiley, New York, 1996).
 4. J. P. Fillard, *Near Field Optics and Nanoscopy* (World Scientific, Singapore, 1996).
 5. E. Betzig, J. K. Trautman, R. Wolfe, E. M. Gyorgy, P. L. Finn, M. H. Kryder, and C.-H. Chang, "Near-field magneto-optics and high density data storage," Appl. Phys. Lett. **61,** 142–144 (1992).
 6. J. Bae, T. Okamoto, T. Fujii, K. Mizuno, and T. Nozokido, "Experimental demonstration for scanning near-field optical microscopy using a metal micro-slit probe at millimeter wavelengths," Appl. Phys. Lett. **71,** 3581–3583 (1997).
 7. O. W. Shih, "Near-field diffraction by a slit in a thick perfectly conducting screen flying above a magneto-optical disk," J. Appl. Phys. **84,** 6485–6498 (1998).
 8. B. D. Terris, H. J. Mamin, D. Rugar, W. R. Studenmund, and G. S. Kino, "Near-field optical data storage using a solid immersion lens," Appl. Phys. Lett. **65,** 388–390 (1994).
 9. B. D. Terris, H. J. Mamin, and D. Rugar, "Near-field optical data storage," Appl. Phys. Lett. **68,** 141–143 (1996).
10. G. S. Kino, "Near-field optical storage," Opt. Photon. News **8**(11), 38–39 (1997).
11. M. Mansuripur and G. Sincerbox, "Principles and techniques of optical data storage," Proc. IEEE **85,** 1780–1796 (1997).
12. M. W. Kowarz, "Diffraction effects in the near field," Ph.D. dissertation (University of Rochester, Rochester, N.Y., 1995).
13. A. Madrazo and M. Nieto-Vesperinas, "Model near field calculations for optical data storage readout," Appl. Phys. Lett. **70,** 31–33 (1997).
14. J. B. Judkins and R. W. Ziolkowski, "Finite-difference time-domain modeling of nonperfectly conducting metallic thin-film grating," J. Opt. Soc. Am. A **12,** 1974–1983 (1995).
15. J. B. Judkins, C. W. Haggans, and R. W. Ziolkowski, "Two-dimensional finite-difference time-domain simulation for rewritable optical disk surface structure design," Appl. Opt. **35,** 2477–2487 (1996).
16. H. Ooki, "Vector diffraction theory for magnetooptical disc systems," Optik **89,** 15–22 (1991).
17. Y.-L. Kok, "Boundary-value solution to electromagnetic scat-

tering by a rectangular groove in a ground plane," J. Opt. Soc. Am. A **9,** 302–311 (1992).

18. K. Kobayashi, "Vector diffraction modeling: polarization dependence of optical read-out/servo signals," Jpn. J. Appl. Phys. **32,** 3175–3184 (1993).

19. T. Park, H. Eom, and K. Yoshitomi, "Analysis of TM scattering from finite rectangular grooves in a conducting plane," J. Opt. Soc. Am. A **10,** 905–911 (1993).

20. O. Mata-Mendez and J. Sumaya-Martinez, "Scattering of TE-polarized waves by a finite grating: giant resonant enhancement of the electric field within the grooves," J. Opt. Soc. Am. A **14,** 2203–2211 (1997).

21. T. Kojima and J. Ido, "Boundary-element method analysis of light-beam scattering and the sum and differential signal output by DRAW-type optical disk models," Electron. Commun. Jpn. Part 2 Electron. **74,** 11–19 (1991).

22. Y. Miyazaki and K. Manabe, "Scattered near-field and induced current of a beam wave by pits on optical disks using boundary element analysis," Radio Sci. **26,** 281–289 (1991).

23. M. Ogawa, M. Nakada, R. Katayama, M. Okada, and M. Itoh, "Analysis of scattering light from magnetic material with land/groove by three-dimensional boundary element method," Jpn. J. Appl. Phys. **35,** 336–341 (1996).

24. K. Hirayama, E. Glytsis, and T. Gaylord, "Rigorous electromagnetic analysis of diffraction by finite-number-of-periods gratings," J. Opt. Soc. Am. A **14,** 907–917 (1997).

25. J. G. Dil and B. A. J. Jacobs, "Apparent size of reflecting polygonal obstacles of the order one wavelength," J. Opt. Soc. Am. **69,** 950–960 (1979).

26. D. S. Marx and D. Psaltis, "Optical diffraction of focused spots and subwavelength structures," J. Opt. Soc. Am. A **14,** 1268–1278 (1997).

27. D. S. Marx and D. Psaltis, "Polarization quadrature measurement of subwavelength diffracting structures," Appl. Opt. **36,** 6434–6440 (1997).

28. R. Depine and D. Skigin, "Scattering from metallic surfaces having a finite number of rectangular grooves," J. Opt. Soc. Am. A **11,** 2844–2850 (1994).

29. W.-C. Liu and M. W. Kowarz, "Vector diffraction from subwavelength optical disk structures: two-dimensional near-field profiles," Opt. Express **2,** 191–197 (1998).

30. R. E. Gerber and M. Mansuripur, "Dependence of the tracking performance of an optical disk on the direction of the incident-light polarization," Appl. Opt. **34,** 8192–8200 (1995).

31. K. D. Paulsen, "Finite-element solution of Maxwell's equations with Helmholtz forms," J. Opt. Soc. Am. A **11,** 1434–1444 (1994).

32. B.-N. Jiang, J. Wu, and L. A. Povinelli, "The origin of spurious solutions in computational electromagnetics," J. Comput. Phys. **125,** 104–123 (1996).

33. P. Concus and G. H. Golub, "Use of fast direct methods for the efficient numerical solution of nonseparable elliptic equations," SIAM (Soc. Ind. Appl. Math.) J. Numer. Anal. **10,** 1103–1120 (1973).

34. B. L. Buzbee, G. H. Golub, and C. W. Nielson, "On direct methods for solving Poisson's equations," SIAM (Soc. Ind. Appl. Math.) J. Numer. Anal. **7,** 627–656 (1970).

35. P. N. Swarztrauber, "The methods of cyclic reduction, Fourier analysis and the FACR algorithm for the discrete solution of Poisson's equation on a rectangle," SIAM (Soc. Ind. Appl. Math.) Rev. **19,** 490–501 (1977).

36. R. A. Sweet, "A cyclic reduction algorithm for solving block tridiagonal systems of arbitrary dimension," SIAM (Soc. Ind. Appl. Math.) J. Numer. Anal. **14,** 706–720 (1977).

37. P. N. Swarztrauber and R. A. Sweet, "Vector and parallel methods for the direct solution of Poisson's equation," J. Comput. Appl. Math. **27,** 241–263 (1989).

38. E. Gallopoulos and Y. Saad, "A parallel block cyclic reduction algorithm for the fast solution of elliptic equations," Parallel Comput. **10,** 143–159 (1989).

39. Y. Saad and M. H. Schultz, "GMRES: a general minimal residual algorithm for solving nonsymmetric linear systems," SIAM (Soc. Ind. Appl. Math.) J. Sci. Stat. Comput. **7,** 856–869 (1986).

40. C. D. Dimitropoulos and A. N. Beris, "An efficient and robust spectral solver for nonseparable elliptic equations," J. Comput. Phys. **133,** 186–191 (1997).

41. B. Engquist and A. Majda, "Absorbing boundary conditions for the numerical simulation of waves," Math. Comput. **31,** 629–651 (1977).

42. B. Engquist and A. Majda, "Radiation boundary conditions for acoustic and elastic wave calculations," Commun. Pure Appl. Math. **32,** 313–357 (1979).

43. G. Mur, "Absorbing boundary conditions for the finite-difference approximation of the time-domain electromagnetic-field equations," IEEE Trans. Electromagn. Compat. **EMC-23,** 377–382 (1981).

44. R. L. Higdon, "Absorbing boundary conditions for difference approximations to the multi-dimensional wave equation," Math. Comput. **47,** 437–459 (1986).

45. R. L. Higdon, "Numerical absorbing boundary conditions for the wave equation," Math. Comput. **49,** 65–90 (1987).

46. K. S. Yee, "Numerical solution of initial boundary value problems involving Maxwell's equations in isotropic media," IEEE Trans. Antennas Propag. **AP-14,** 302–307 (1966).

47. J. J. Grefet, A. Sentenac, and R. Carminati, "Surface profile reconstruction using near-field data," Opt. Commun. **116,** 20–24 (1995).

48. A. Madrazo and M. Nieto-Vesperinas, "Surface structure and polariton interactions in the scattering of electromagnetic wave from a cylinder in front of a conducting grating: theory for the reflection photon scanning tunneling microscope," J. Opt. Soc. Am. A **13,** 785–795 (1996).

49. G. Bouwhuis, J. Braat, A. Huijser, J. Pasman, G. van Rosmalen, and K. S. Immink, *Principles of Optical Disc Systems* (Hilger, Bristol, UK, 1985).

50. A. B. Marchant, *Optical Recording: A Technical Overview* (Addison-Wesley, Reading, Mass., 1990).

51. M. Mansuripur, *The Physical Principles of Magneto-Optical Recording* (Cambridge U. Press, New York, 1995).